


Phase-field modeling of γ/γ'' microstructure formation in Ni-based superalloys with high γ'' volume fraction

Felix Schleifer, Markus Holzinger, Yueh-Yu Lin, Uwe Glatzel, and Michael Fleck*

Metals and Alloys, University of Bayreuth, Prof.-Rüdiger-Bormann-Str. 1, 95447 Bayreuth, Bavaria, Germany

The excellent mechanical properties of the Ni-based superalloy IN718 mainly result from coherent γ'' precipitates. Due to a strongly anisotropic lattice misfit between the matrix and the precipitate phase, the particles exhibit pronounced plate-shaped morphologies. Using a phase-field model, we investigate various influencing factors that determine the equilibrium shapes of γ'' precipitates, minimizing the sum of the total elastic and interfacial energy. Upon increasing precipitate phase fractions, the model predicts increasingly stronger particle-particle interactions, leading to shapes with significantly increased aspect ratios. Matching the a priori unknown interfacial energy density to fit experimental γ'' shapes is sensitive to the phase content imposed in the underlying model. Considering vanishing phase content leads to 30% lower estimates of the interfacial energy density, as compared to estimates based on realistic phase fractions of 12%. We consider the periodic arrangement of precipitates in different hexagonal and rectangular superstructures, which result from distinct choices of point-symmetric and periodic boundary conditions. Further, non-volume conserving boundary conditions are implemented to compensate for strains due to an anisotropic lattice mismatch between the γ matrix and the γ'' precipitate. As compared to conventional boundary conditions, this specifically tailored simulation configuration does not conflict with the systems periodicity and provides substantially more realistic total elastic energies at high precipitate volume fractions. The energetically most favorable superstructure is found to be a hexagonal precipitate arrangement.

© 2020. The manuscript is made available under the license [CC-BY-NC-ND 4.0](https://creativecommons.org/licenses/by-nc-nd/4.0/) 

INTRODUCTION

Ni-based superalloys have various applications at elevated temperatures, especially in stationary gas turbines and airplane engines. The main strengthening mechanism, which makes these alloys applicable for high temperatures is particle strengthening by coherent precipitations [1]. Apart from the most prominent case, the γ' strengthening of Ni-based superalloys for turbine blade materials, a series of alloys exist that are mainly strengthened by the tetragonal metastable γ'' phase. These Nb-containing alloys, such as the well-known IN718, can be cast, forged, machined and welded which renders them ideal candidates for industrial applications.

As IN718 contains up to 6% of the cubic $L1_2$ phase γ' , several authors modified its composition in order to increase the volume fraction of γ'' phase and to get rid of γ' precipitates while maintaining the composition of the matrix [2–5]. Table I shows the nominal composition of IN718 and a derivative IN718M without γ' forming elements. Recent studies aim at deliberate co-precipitation of γ' and γ'' to exploit ripening inhibiting effects [6, 7] and a dual lattice microstructure [8, 9]. IN718 powders also gain importance for additive manufacturing in the industrial environment [10–13]. It was recently found that alloys containing only one orientational variant of γ'' , a so-called single-variant microstructure, can be used to tailor creep resistant materials [14].

Figure 1a) shows a scanning electron microscope (SEM) image of a γ/γ'' microstructure in IN718M after homogenization at 1423K for 2h. The precipitates

are found in the Nb-rich interdendritic region. Table I also shows the local composition measured by energy-dispersive x-ray spectroscopy. The precipitates are arranged regularly in three spatial orientations perpendicular to one another and show a plate-shaped morphology. The volumetric γ'' phase fraction is $\geq 12\%$. Figure 1b) shows a dark-field transmission electron microscope (TEM) image of γ'' precipitates in IN718M.

Composition in wt. %	Ni	Cr	Nb	Mo	Fe	Al	Ti
IN718 nominal max.	55.0	21.0	5.5	3.3	bal.	0.8	1.2
IN718 nominal min.	50.0	17.0	4.8	2.8	bal.	0.2	0.7
IN718M nominal	58.0	18.0	5.0	3.0	bal.	–	–
IN718M measured	56.8	17.6	6.6	3.2	15.8	–	–

Table I. Nominal composition in wt. % of IN718 and its derivative IN718M together with the measured composition in the Nb-rich region of IN718M as shown in Figure 1a).

The shapes and spatial arrangements of coherent misfitting precipitates have been modeled assuming a single precipitate embedded in infinite matrix [15–21]. The influence of elastic inhomogeneity [22] and periodic arrangements of precipitates with higher precipitate volume fractions [23] on precipitate shapes were studied using the boundary integral method. Comparison of simulated precipitate shapes to experimentally observed microstructures can be used to obtain realistic values of the interfacial energy density [24–26].

The phase-field method is widely considered to be a powerful tool for modeling solidification as well as solid-state phase transformations based on a diffuse descrip-

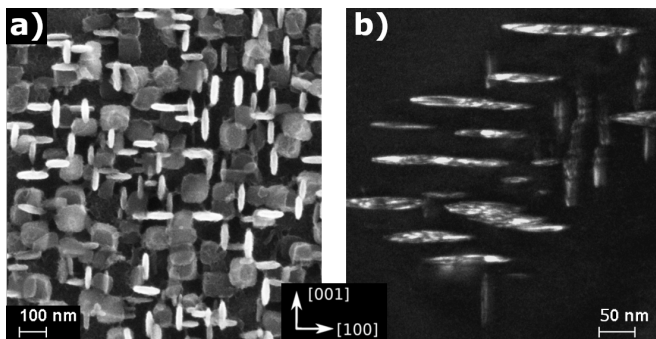


Figure 1. a) Scanning electron microscopy (SEM) image of a γ/γ'' microstructure in the Nb-rich region of IN718M (composition given in Table I). The orientational variants of the γ'' precipitates are clearly distinguishable. b) Dark-field transmission electron microscopy (TEM) image of γ'' precipitates in IN718M.

tion of the phase boundaries [27–31]. Consistent phase-field modeling of precipitation bases on a thermodynamic functional, which is an integral over a local phenomenological potential energy density. This phenomenological energy density may take into account phase boundary energy, multi-component solute distribution and elastic strain caused by external loads or lattice misfit between the phases. By general variational principles, one can subsequently derive a consistent set of coupled partial differential equations that describes the kinetics of the microstructure evolution in the chosen configuration. The phase-field method is frequently used to study the temporal evolution of γ/γ'' microstructures [32–37] as well as γ/γ'' systems [38, 39]. The variational formulation of the phase-field method makes it a useful tool to determine equilibrium precipitate morphologies [40–45] and precipitate interactions [46]. In the scope of this work, we develop a phase-field model to extensively evaluate factors influencing two-dimensional γ'' precipitate shapes. We consider anisotropic and phase-dependent elastic properties, a tetragonally anisotropic misfit, elastic particle interactions at high volume content as well as an isotropic energy density of the γ/γ'' interface.

THE Γ/Γ'' MICROSTRUCTURE IN NI-BASED SUPERALLOYS

The ordered $D0_{22}$ phase γ'' has a body-centered tetragonal (bct) crystallographic structure and is of the stoichiometric type Ni_3Nb . In an fcc matrix, it forms distinctive plate-shaped precipitates. The face-centered cubic (fcc) unit cell of the matrix phase γ can be described by a single lattice parameter a_γ that is the distance between two atom sites along a $\langle 100 \rangle$ direction. The bct unit cell of the γ'' phase can be made up by two fcc unit cells stacked on top of each other with the central atom site and the corner atom sites being Nb atoms. One can

now distinguish two lattice parameters $a_{\gamma''}$ and $c_{\gamma''}$, the latter being also referred to as the tetragonal axis. The plate normal of the precipitate is always parallel to the $c_{\gamma''}$ direction.

Coherent precipitation of γ'' in a γ matrix is possible due to the relations

$$\begin{aligned} a_{\gamma''} &\approx a_\gamma \\ c_{\gamma''} &\approx 2a_\gamma, \end{aligned} \quad (1)$$

when

$$\langle 100 \rangle_\gamma \parallel \langle 100 \rangle_{\gamma''}. \quad (2)$$

This means that there are three possible orientational variants in which the tetragonal phase can coherently precipitate (see Figure 1) [47]. Note that Equation (1) states that there is a misfit of the lattice parameters that leads to strains when lattice coherency is kept. Two distinguishable misfit strains ε_1 and ε_3 in $a_{\gamma''}$ and $c_{\gamma''}$ direction, respectively, can be found.

Figure 2 shows a schematic drawing of a γ'' precipitate. The precipitate is depicted as an oblate spheroid with two major and a minor half axis R and r , respectively. The orientational relations given in Equation (2) are depicted at the interface. To experimentally quantify the shape of γ'' precipitates one usually takes the aspect ratio that is defined as the ratio R/r or, for non-elliptical precipitates the ratio of the plate diameter to its thickness. Usually, γ'' precipitates exhibit major radii of less than 130 nm and reportedly start to lose full coherency at major radii larger than 25 nm [25, 39, 48, 49].

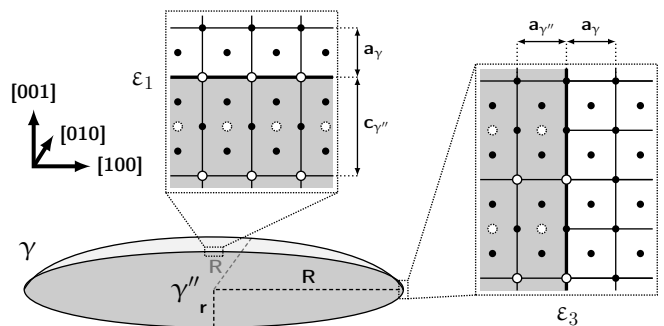


Figure 2. Cut through the center of a γ'' precipitate (gray) parallel to the (010) plane. The two major half axes R and the minor half axis r of the precipitate are indicated by dashed lines. The two orientations of the respective unit cells in the interface are shown that lead to two distinguishable misfit strains ε_1 and ε_3 . Black circles indicate Ni atoms and white ones Nb, respectively. Dotted Nb atoms lie below the cut plane. The lattice parameters a_γ , $a_{\gamma''}$ and $c_{\gamma''}$ are also indicated.

Elastic constants

General elastic behavior is described by the tensor of elasticity C_{ijkl} . In this work, we use the tensor of elastic-

ity in Voigt notation C_{ij} . This is a reduction to a 6×6 tensor that is not invariant under rotation. The cubic γ and the tetragonal γ'' phase both exhibit anisotropic elastic properties due to their crystallographic symmetry. A set of three independent elastic constants is needed to describe cubic anisotropy (C_{11} , C_{12} , C_{44}) and six are needed for tetragonal anisotropy, respectively (C_{11} , C_{33} , C_{12} , C_{13} , C_{44} , C_{66}). Isotropic elasticity is described by a set of two independent constants with $C_{11} = 2C_{44} + C_{12}$.

In this work we use experimental data generated by resonance ultrasound spectroscopy (RUS) for polycrystal (isotropic) and single crystal (anisotropic) samples of IN718. We assume that matrix and precipitates in IN718 and IN718M have comparable elastic properties. For the γ'' phase data from a first-principles study was used [50, 51]. This data is valid at 0 K, therefore, an estimate about temperature dependence has to be made. Due to the lack of experimental data, we propose to assume the same temperature dependence for all elastic constants considered, as it was already done by Moore et al. [52]. In this work, we assume a linear temperature dependence of the elastic constants

$$C_{ij}(T) = C_{ij}^{0K}(1 - \beta\Delta T), \quad (3)$$

where T is the temperature, C_{ij}^{0K} is an elastic constant at 0 K and β is the coefficient of temperature dependence. To determine β , experimental data for pure Nickel from 0 K to room temperature is used [53, 54]. For higher temperatures, we assume the same temperature dependence as it was determined for a γ' single crystal (Ni-Al23-Ti1-Ta1) via RUS [55]. We find β to be $2.3 \cdot 10^{-4} \text{ K}^{-1}$. Table II shows the extrapolated elastic constants of γ'' at 998 K. Elastic homogeneity is given when matrix and precipitate have the same tensor of elasticity ($C_{ij}^\gamma = C_{ij}^{\gamma''}$).

The elastic constants of a single crystal alloy composed of N coherent phases can be estimated by a simple rule of mixture

$$\bar{C}_{ij} = \sum_{\alpha} C_{ij}^{\alpha} V_{\alpha}, \quad (4)$$

where \bar{C}_{ij} is an elastic constant of the alloy, C_{ij}^{α} is the elastic constant of phase α and V_{α} is the volume fraction of α . Knowing the elastic properties for all but one phase and for the alloy itself, it is possible to estimate the tensor of elasticity for the remaining phase. In the case of γ'' precipitates in a cubic matrix, the three orientational variants appear statistically. The tensor of elasticity of such an alloy maintains cubic symmetry. To find the tensor of elasticity, with cubic symmetry, for a mixture of all three orientation variants $\bar{C}_{ij}^{\gamma''}$ of the γ'' phase, we apply

the modified mixture rule

$$\bar{C}_{11}^{\gamma''} = (2C_{11}^{\gamma''} + C_{33}^{\gamma''})/3 \quad (5)$$

$$\bar{C}_{12}^{\gamma''} = (C_{12}^{\gamma''} + 2C_{13}^{\gamma''})/3 \quad (6)$$

$$\bar{C}_{44}^{\gamma''} = (2C_{44}^{\gamma''} + C_{66}^{\gamma''})/3. \quad (7)$$

Having estimated the complete tensors of elasticity for the IN718M alloy and the γ'' phase, the anisotropic tensor of elasticity of the matrix can be calculated using Equation (4) and (7). In Table II also a stiffness contrast $C_{ij}^{\gamma''}/C_{ij}^{\gamma}$ is given. In the case of anisotropic elasticity, we apply the mixture rule in Equation (7) to compare the respective tensors of elasticity. We report a mean value as the different elastic constants show different stiffness contrasts.

To evaluate the influence of inhomogeneous stiffness of the phases and of crystallographic anisotropy on the precipitate shapes, we use different sets of elastic constants. Phase-independent isotropic elastic properties leave only the anisotropic lattice misfit to determine the precipitate shape. Phase-wise isotropic data allows to observe the influence of elastic inhomogeneity. Individual cubic and tetragonally anisotropic phase data describes the elastic properties of the system in the most comprehensive way.

		elastic constants in GPa						contrast
		C_{11}	C_{33}	C_{12}	C_{13}	C_{44}	C_{66}	$C_{ij}^{\gamma''}/C_{ij}^{\gamma}$
isotropic	homogen. ¹	(242)		120		61		1.0
	matrix ³	(240)		120		60		} < 1.1
	γ'' phase ⁴	(250)		120		65		
anisotropic	homogen. ¹	205		145		90		1.0
	matrix ³	200		150		90		} \approx 0.9
	γ'' phase ²	220	240	140	120	88	87	

Table II. Elastic constants at 998 K used in this work. Data for the individual phases and for an elastically homogeneous system ($C_{ij}^{\gamma} = C_{ij}^{\gamma''}$) are provided as well as isotropic and anisotropic data sets to evaluate respective effects separately. Values of a mean stiffness contrast $C_{ij}^{\gamma''}/C_{ij}^{\gamma}$ are provided. Data is generated via: ¹resonance ultrasound spectroscopy ²first-principles calculations [50, 51] and Equation (3) ³Equation (4) ⁴Equation (7)

All evaluations of the elastic moduli of the phases based Equation (4) are dependent on the volume fraction V_{α} . In this work, we assume a γ'' volume fraction of 12% which is in accordance with previously reported values [56, 57] and higher than it was calculated using the Thermo-Calc software with the TCNi8 database.

Anisotropic lattice misfit

Due to the two distinguishable lattice parameters a and c in γ'' and the strict orientation relation of the coherent interface in a γ/γ'' microstructure the stress-free transformation strain ε_{ij}^0 exhibits a tetragonal symmetry. In Voigt notation, this misfit strain tensor ε_0 of the γ'' phase is

$$\varepsilon_0 = (\varepsilon_1, \varepsilon_1, \varepsilon_3, 0, 0, 0)^T, \quad (8)$$

with the two distinguishable dilatational misfit strains ε_1 and ε_3 . Those are calculated from the experimentally determined lattice parameters of the phases via

$$\varepsilon_1 = \frac{a_{\gamma''} - a_{\gamma}}{a_{\gamma}}, \quad \varepsilon_3 = \frac{c_{\gamma''} - 2a_{\gamma}}{2a_{\gamma}}. \quad (9)$$

Note that in the denominator we find only the lattice parameter of the matrix. This is because we define the eigenstrain of the matrix to be zero. The lattice parameters of an IN718 matrix and of the γ'' precipitates were measured by Slama et al. [47, 49] using X-ray diffractometry (XRD) for samples aged at 953 K and 1023 K after quenching. Lattice parameters were also measured using neutron diffraction [58]. Measured lattice parameters and corresponding misfit strains are given in Table III. Other measurements of the lattice parameters in IN718 show similar misfits [4, 48, 59–62]. Note that the absolute value of ε_3 is high compared to γ' precipitates ($\varepsilon_0^{\gamma'} \approx -1 \dots -3 \cdot 10^{-3}$ [63]) but similar for both XRD and neutron diffraction. On the other hand, the values of ε_1 differ strongly. The misfit ratio $\varepsilon_3/\varepsilon_1$ is one magnitude larger for neutron diffraction measurements than for the XRD measurements.

Both measurements, however, determined the in-situ constrained misfit that is the lattice misfit superimposed by elastic deformation of the material. A more suiting input parameter would be the unconstrained misfit that is the misfit calculated from lattice parameters of strain-free bulk samples of the phases. The unconstrained misfit can notably differ from the constrained misfit [64, 65].

source	lattice param. in pm			misfit in 10^{-3}		
	a_{γ}	$a_{\gamma''}$	$c_{\gamma''}$	ε_1	ε_3	$\varepsilon_3/\varepsilon_1$
[47, 49]	359.5	361.4	742.1	5.29	32.1	6.1
[58]	359.8	360.0	743.8	0.56	33.6	60.0

Table III. Lattice parameters from literature for an IN718 matrix and γ'' precipitates. Misfit strains are given according to Equation (9) as well as the respective misfit ratio $\varepsilon_3/\varepsilon_1$.

PHASE-FIELD MODELING OF EQUILIBRIUM PRECIPITATE SHAPES

The phase-field model for the simulation of solid-phase precipitation in multicomponent alloys is based on the following phenomenological potential functional [35, 66, 67],

$$\Omega = \int_V \omega(\varphi, \{\partial_i \varphi\}, \{\partial_k u_i\}) dV, \quad (10)$$

where ∂_i denotes an abbreviation for the partial derivative with respect to the spacial directions $i = x, y, z$, e.g. $\partial_x \equiv \partial/\partial x$. The potential density ω splits into an interfacial, a bulk elastic contribution and a chemical contribution $\omega = \omega_{\text{int}} + \omega_{\text{el}} + \omega_{\text{ch}}$. The continuous fields describing the evolution of the system are the phase-field φ , which discriminates between the fcc matrix ($\varphi = 0$) and the ordered γ'' phase ($\varphi = 1$) as well as the elastic displacement field $\{u_i\} = (u_x, u_y, u_z)$, which describes the local distortion of a material point by elastic deformations.

Interfacial contribution

The interfacial contribution to the potential functional is

$$\omega_{\text{int}} = \frac{\Gamma \xi}{\Gamma_0} (\partial_i \varphi \partial_i \varphi) + \frac{\Gamma}{\xi \Gamma_0} p(\varphi), \quad (11)$$

where a summation over repeated indices is implied. The phase-field parameter ξ determines the interface width and the parameter Γ corresponds to the interfacial energy density. Γ_0 denotes a calibration factor for the interface energy density, which is calculated via the line integral, $\Gamma_0 = \int \omega_{\text{int}}(\varphi_0, \{\partial_i \varphi_0\}) dn / \Gamma$, where n denotes the direction normal to the interface, and φ_0 is a phase-field with just one full transition from $\varphi = 0$ to $\varphi = 1$. Further, the equilibrium potential is

$$p(\varphi) = \frac{\xi^2}{\Delta x^2} \left\{ \varphi(1-\varphi) + \frac{1-a^2}{4a^2} \log \left(\frac{1-a^2}{1-a^2(1-2\varphi)^2} \right) \right\}, \quad (12)$$

where the parameter $a = \tanh(2\Delta x/\xi)$ couples to the discretization grid via the numerical grid spacing Δx . This potential has two local minima at $\varphi = 0$ and $\varphi = 1$, which correspond to the two distinct phases of the system. In the continuum limit $\Delta x \rightarrow 0$, this potential converges to the usual quartic double-well potential $p_{\infty}(\varphi) = 8\varphi^2(1-\varphi)^2$, as $\lim_{\Delta x \rightarrow 0} \xi^2 a^2 / \Delta x^2 = 4$.

Figure 3 shows the equilibrium potential for $\xi/\Delta x = 2$, which will be used throughout this work as well as for the continuum limit $\xi/\Delta x \rightarrow \infty$. The reason for choosing this potential is to diminish effects from the

numerical grid in the phase-field model, according to the ideas around the so-called ‘‘Sharp phase-field method’’ as proposed by Finel et al. [68, 69].

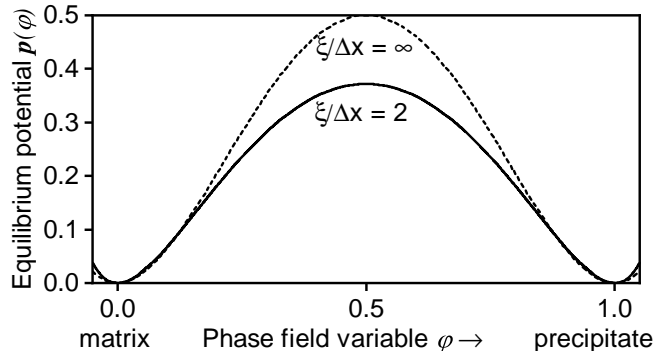


Figure 3. Plot of the equilibrium potential given in Equation (3) as a function of the phase-field variable φ for different values of $\xi/\Delta x$.

In conjunction with the formulation of the interfacial contribution, we impose an interpolation function $h(\varphi) = \varphi^2(3 - 2\varphi)$ for any elastic and chemical energy density contribution: $\omega_{el} + \omega_{ch} = \omega_{el}(h(\varphi)) + \omega_{ch}(h(\varphi))$. This is the minimal polynomial satisfying the necessary interpolation conditions $h(0) = 0$ and $h(1) = 1$ and also having a vanishing slope at $\varphi = 0$ and $\varphi = 1$, to not shift the bulk states in the presence of finite driving forces [70, 71]. The Allen Cahn-type phase-field evolution equation is

$$\begin{aligned} \frac{\partial \varphi}{\partial t} &= -\frac{2M}{3\Gamma\xi} \frac{\delta \Omega}{\delta \varphi} = \frac{2M}{3\Gamma\xi} \left(\partial_i \frac{\partial \omega}{\partial (\partial_i \varphi)} - \frac{\partial \omega}{\partial \varphi} \right) \\ &= M \left(\frac{2}{3\Gamma_0} \left\{ (\partial_i \partial_i) \varphi - \frac{1}{\xi^2} \frac{\partial p(\varphi)}{\partial \varphi} \right\} - \frac{2}{3\Gamma\xi} \frac{\partial h}{\partial \varphi} \left(\frac{\partial \omega_{el}}{\partial h} \right) \right), \end{aligned} \quad (13)$$

where M is the interface mobility that is chosen as high as possible while still guaranteeing stability of the solver. All these equations are solved by finite difference schemes operating on one fixed square grid with an explicit Euler-type time integration.

Elastic contribution

The elastic contribution to the potential energy density ω_{el} is defined in terms of the phase-dependent elastic properties: the total strain field ε that is derived from the local displacements u_i , the misfit strain ε_0 of the precipitate phase, and the phase-dependent elastic constants \bar{C} [55]. Specifically the elastic energy density is written as

$$\omega_{el}(\varphi, x) = \frac{1}{2} (\varepsilon - \bar{\varepsilon}_0) \bar{C} (\varepsilon - \bar{\varepsilon}_0). \quad (14)$$

The phase dependent elastic constants \bar{C}_{ij} as well as the eigenstrains $\bar{\varepsilon}_{0,i}$ are interpolated as

$$\bar{C}_{ij}(\varphi) = \sum_{\alpha} h(\varphi) C_{ij}^{\alpha} \quad (15)$$

$$\bar{\varepsilon}_{0,i}(\varphi) = \sum_{\alpha} h(\varphi) \varepsilon_{0,i}^{\alpha}, \quad (16)$$

where α denotes the considered phase and φ denotes the local phase-field parameter. We interpolate on the level of the elastic parameters, not on the level of the bulk energies to minimize the amount of interfacial excess energy [72]. A Lagrangian formulation in the small strain approximation is used. The local stress tensor is defined as the partial derivative of the elastic energy density Equation (14) with respect to the strain tensor,

$$\sigma = \frac{\partial \omega_{el}}{\partial \varepsilon} = \bar{C} (\varepsilon - \bar{\varepsilon}_0). \quad (17)$$

The solution for the elastic displacement field is given by the condition of mechanic equilibrium

$$\frac{\delta \Omega}{\delta u_i} = \frac{\partial}{\partial x_i} \frac{\partial \omega_{el}}{\partial \varepsilon} = \frac{\partial \sigma}{\partial x_i} = 0, \quad (18)$$

In summary, the model requires to solve the full set of coupled partial differential equations of second order, as given by Equation (13) for the phase-field and Equation (18) for the elastic displacements. With regard to the mechanical equilibrium, that is assumed at every time step of the phase-field solver, we perform a Jacobi relaxation.

Chemical contribution

Realistic microstructure exhibit conserved phase volumes, due to the conservation of mass [55]. Here, the preserved phase volume is achieved by the chemical contribution to the potential energy density

$$\omega_{ch}(t) = h(\varphi) f_{ch}(t), \quad (19)$$

which contains an extra time-dependent and homogeneous driving force contribution $f_{ch}(t)$, such that a volume change of the precipitate phase is prohibited [73]. A more sophisticated description of the kinetics of diffusion-limited precipitation, which explicitly involves the chemical diffusion of multiple alloying elements, is also possible [55, 67], but beyond the scope of the present work.

The phase fraction V_{α} is conserved when

$$0 = \frac{d}{dt} V_{\alpha}(t) = \int_V \frac{\partial}{\partial t} \varphi(\mathbf{x}, t) dV. \quad (20)$$

Inserting the right-hand side of phase-field Equation (13) into (20), we obtain the time-dependent homogeneous driving force

$$f_{ch}(t) = \frac{3\Gamma\xi}{2} \frac{G(t)}{H(t)}, \quad (21)$$

where the following abbreviations are introduced:

$$G(t) = \int_V \left(\partial_i (\partial_i \varphi) - \frac{8}{\xi^2} \frac{\partial p(\varphi)}{\partial \varphi} - \frac{2}{3\Gamma\xi} \frac{\partial \omega_{el}}{\partial \varphi} \right) dV, \quad (22)$$

$$H(t) = \int_V \frac{\partial h}{\partial \varphi} dV. \quad (23)$$

This method for achieving preserved phase volumes can also be applied to configurations involving more than two phases [74].

Boundary conditions

All simulations are carried out in rectangular two-dimensional domains. Elastic interactions between neighboring precipitates can be adjusted by changing the domain size with respect to the size of the initial precipitate. For both cubic and tetragonal symmetry, it is sufficient to model one quarter of the particle with respective mirror boundary conditions. Therefore, for every considered spatial dimension exists one mirror boundary and one opposing domain boundary that ensures periodicity (henceforth referred to as the periodic boundary). The phase-field is imposed with no-flux boundary conditions in both cases.

For the elastic displacement fields, standard boundary conditions such as periodic conditions, strain-free conditions or stress-free boundary conditions are not useful. Here, a distinction is required due to the following reasons. If simple stress-free condition are imposed the state of deformation turns non-uniform, and the boundary loses its flatness, which conflicts with the periodicity of the system. Periodic or strain-free conditions conserve periodicity, but do not allow for the misfitting precipitate to change the volume of the simulation domain and/or its aspect ratio, leading to unrealistically high total deformation energies.

Therefore, at the mirror boundaries vanishing normal displacements $u_n = 0$ and vanishing shear strains $\partial u_t / \partial n = 0$ are imposed, where \mathbf{u} denotes the elastic displacement field, n and t denote the direction normal and tangential to the boundary, respectively. At the opposing periodic boundary again vanishing shear strain conditions are imposed. But for the normal displacement, we homogeneously impose $u_n = \bar{u}_n$, where \bar{u}_n denotes the average value of all normal displacements at the boundary. Homogeneous normal displacements are required to avoid conflicts with the periodicity of the systems and to not introduce strain artifacts. The average overall normal displacements at the boundary is used to allow for the volume change, which leads to more realistic total deformation energies. This boundary condition has previously been applied to finite-element modeling of misfit stresses [75–78] and equilibrium shapes [23] in the γ/γ' system. Due to these boundary conditions, all opposing

domain boundaries stay parallel yet no spurious elastic energy is introduced through artificial volume conservation.

Figure 4a) shows a simulation domain with an aspect ratio of 2.5 and the imposed boundary conditions for the displacements normal to the boundaries. Modeling a precipitate in a periodic configuration implies an arrangement of the precipitates in a strict long-range order. Specifically, the above boundary conditions imply a superstructure in which the precipitates are arranged in the corners of a cuboidal unit-cell [23] with the distance to each nearest neighbor being twice the domain side lengths. Henceforth this configuration will be referred to as a rectangular superstructure.

By application of antisymmetric variation boundary conditions at one periodic boundary, one can change the arrangement superstructure [79]. Therefore the tangential strains and the phase-field must be imposed with a point-symmetric operation with respect to a bisecting point of the respective domain boundary. Figure 4b) shows the rectangular superstructure and Figure 4c) and d) show two hexagonal arrangements henceforth referred to as hexagonal_x and hexagonal_y. The respective bisecting point that is used for the antisymmetry operation is indicated as a red dot. Antisymmetric boundary conditions applied to more than one boundary lead to virtual simulation domains that include more than one precipitate. This state is not represented by the actual simulation domain and renders non-physical solutions.

SIMULATION RESULTS AND DISCUSSION

To determine the shape of coherent γ'' precipitates we set up phase-field simulations considering the interfacial energy and elastic contributions with constant γ'' phase fraction. Beginning from an arbitrary precipitate shape the phase-field converges towards the minimum of the total energy. The lower left edge of the domain lies in the precipitates center point with the domain boundaries being parallel to the crystallographic [100] and [001] directions. The observed phase fraction in two dimensions appears higher than the respective three-dimensional phase fraction. Beginning from the discussed initial simulation configuration the system was relaxed for a minimum of $4 \cdot 10^5$ iterations. Subsequently the aspect ratio and the total energy contributions were evaluated.

To describe the ratio between interfacial and elastic contribution to the pattern formation we introduce a dimensionless parameter L similar to the one presented in [18] as

$$L = \frac{lC_{44}\varepsilon_3^2}{\Gamma}, \quad (24)$$

where $C_{44}\varepsilon_3^2$ is the elastic energy density scale with the shear modulus C_{44} of the homogeneous isotropic elastic

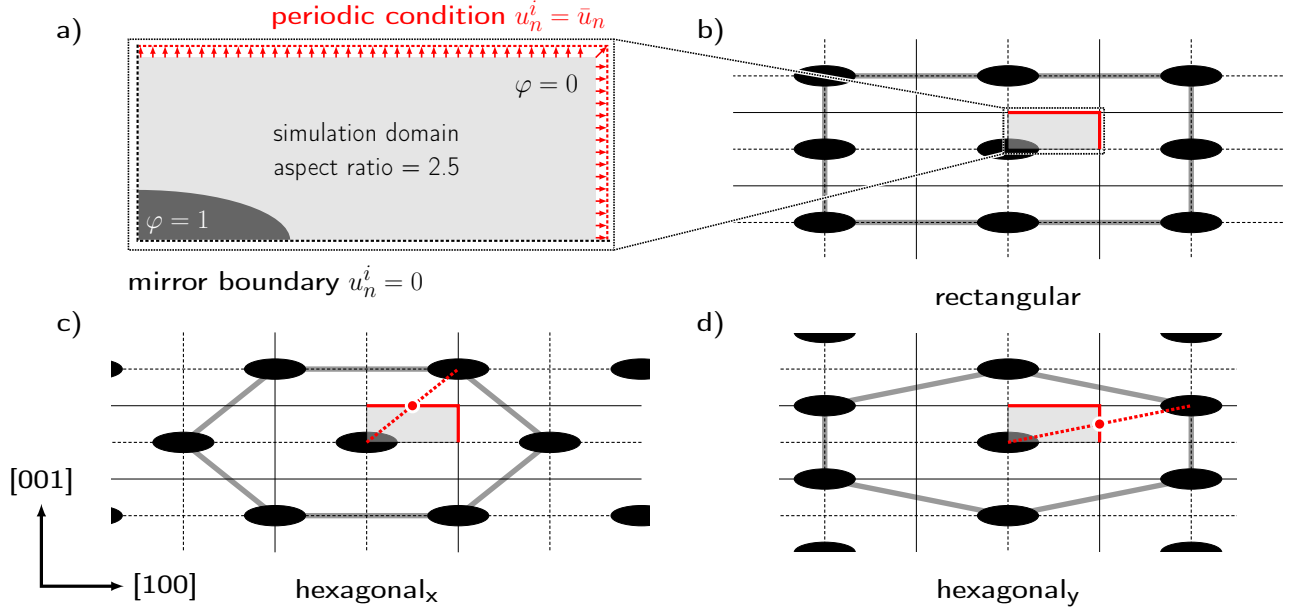


Figure 4. a) Rectangular simulation domain. The specifically tailored boundary conditions for the displacements normal to the boundaries are indicated in red. Mirror boundaries are indicated by dashed lines and the periodic boundary conditions that allow for volume change of the domain are indicated by solid red lines, respectively. b) The implied rectangular precipitate superstructure. c) and d) Precipitate arrangements hexagonal_x and hexagonal_y that arise from point symmetry centers indicated by a red dot.

data provided in Table II and the largest misfit strain ε_3 from Table III to make it independent of the misfit ratio $\varepsilon_3/\varepsilon_1$. Γ is the isotropic interfacial energy density. The length scale of a particle is defined as $l = \sqrt{Rr}$ and will be used to normalize lengths. R denotes the major half axes and r the minor half axis of the precipitate, as shown in Figure 2 on page 2.

Variation of anisotropic misfit and elastic constants

To evaluate the influence of the anisotropy of the misfit strains given in Table III, the simulation domain was chosen to be 50×50 gridpoints with one quarter of an initial, spherical particle with a 10 gridpoint radius in the bottom left corner. The low phase content together with homogeneous and isotropic elastic material data leaves only the misfit ratio $\varepsilon_3/\varepsilon_1$ and the interfacial energy density Γ to determine the equilibrium shape. In this configuration the tetragonal symmetry of the misfit strain is the cause of the plate shape of the γ'' precipitates. There is significant uncertainty about the absolute values of the lattice misfit strain ε_1 (see Table III). The misfit strain ε_3 is fixed to a value of $30 \cdot 10^{-3}$ and $\varepsilon_3/\varepsilon_1$ is varied to examine the influence of the anisotropy of the misfit $\varepsilon_3/\varepsilon_1$ on the precipitate shape.

Figure 5a) shows the precipitate aspect ratio as determined by the phase-field model as a function of the misfit ratio $\varepsilon_3/\varepsilon_1$. At $\varepsilon_3/\varepsilon_1 = 1$ the precipitates are cir-

cular with an aspect ratio of 1. With rising misfit ratio the precipitates show elliptical shapes with an aspect ratio that rises until a plateau is reached. In the plateau region, changes in the misfit ratio do no longer influence the precipitate shape. For all considered values of L the plateau is reached at $\varepsilon_3/\varepsilon_1 \geq 3$. The misfit data considered in Table III lies between $\varepsilon_3/\varepsilon_1 = 6$ and 60 and thus lies inside the plateau region.

In Figure 5a) the simulations are compared to an analytical model for the optimum shape of γ'' precipitates. The shape is assumed to be a rotational ellipse with an aspect ratio A . The elastic energy density e is homogeneous inside the precipitate and can be calculated using Eshelby's solution to the inclusion problem [80] as

$$e = \frac{C_{44}}{1 - 2\nu} (\beta_1 \varepsilon_1^2 + \beta_2 \varepsilon_1 + \beta_3 \varepsilon_1 \varepsilon_3), \quad (25)$$

where $2\nu = C_{12}/(C_{12} - C_{44})$ and the parameters β_i only depend on the aspect ratio of the ellipsoid [25, 48]. The optimum aspect ratio is then the aspect ratio that minimizes the sum of elastic energy and interface energy as follows

$$\frac{\partial}{\partial A} (\Gamma S_0 + e V_0) = 0, \quad (26)$$

with $S_0(R, A)$ and $V_0(R, A)$ being the surface and volume of an oblate rotational ellipse with major radius R and aspect ratio A [48]. The aspect ratios determined by the phase-field model and by the analytical model are very

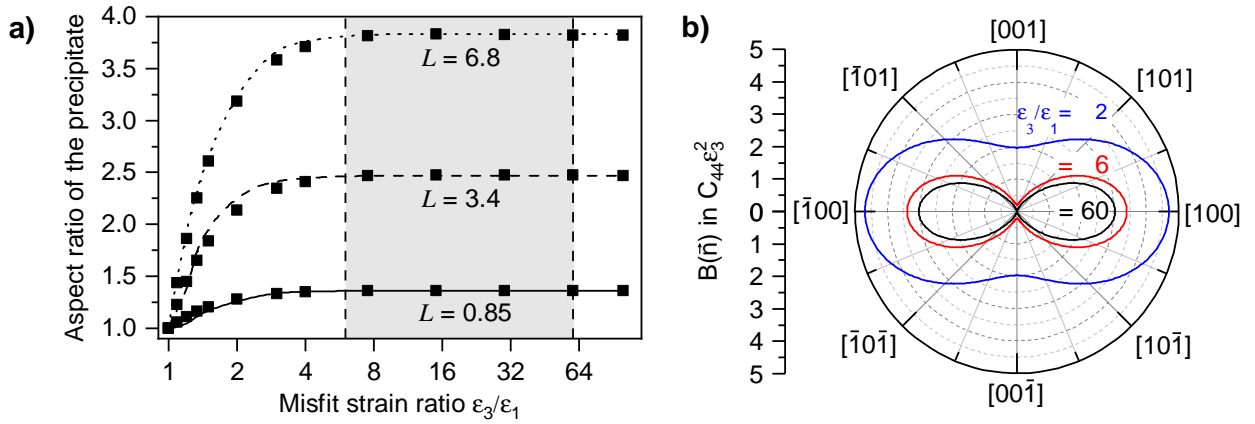


Figure 5. a) Precipitate aspect ratio as a function of the misfit ratio $\varepsilon_3/\varepsilon_1$ for three different L considering homogeneous and isotropic elasticity without elastic interaction with neighboring precipitates. The range in which realistic values for γ'' lie is indicated in gray (see Table III). Symbols are phase-field results and the lines are taken from the model given in Equation (25) and (26). b) Polar plots of the elastic energy function $B(\vec{n})$ for different orientations of the interface normal \vec{n} in the (010) plane and different misfit ratios $\varepsilon_3/\varepsilon_1$.

close and the analytic model shows the same plateau for large misfit ratios.

Figure 5b) shows the orientation dependent elastic relaxation function $B(\vec{n})$ that quantifies soft and hard crystallographic directions independent of the precipitate shape [15, 46, 81]. It is defined as

$$\begin{aligned} B(\vec{n}) &= C_{ijkl}\varepsilon_{ij}^0\varepsilon_{kl}^0 - n_i\sigma_{ij}^0G_{jk}(\vec{n})\sigma_{kl}^0n_l \\ \sigma_{ij}^0 &= C_{ijkl}\varepsilon_{kl}^0 \\ G_{jk}^{-1}(\vec{n}) &= C_{ijkl}n_in_l \end{aligned} \quad (27)$$

with implied summation over repeated indices. The elastic properties are assumed to be homogeneous and isotropic (see Table II) and only $\varepsilon_3/\varepsilon_1$ is varied. For $\varepsilon_3/\varepsilon_1 > 1$ the direction minimizing $B(\vec{n})$ has been found to be the tetragonal axis ([001]) [82]. Assuming vanishing interfacial energy density the equilibrium precipitate shape is an infinitely extended plate with a ([001]) habit plane [81, 82]. Finite interfacial energy contributes significantly to the formation of the experimentally observed shapes by counteracting this strong anisotropy driving force of $B_{[100]}/B_{[001]} \gg 1$ that is observed for $\varepsilon_3/\varepsilon_1 = 6$ and 60. For $\varepsilon_3/\varepsilon_1 \gg 1$ the precipitate aspect ratio is influenced only by L and the contribution of ε_1 is therefore negligible. In Figure 5b), for $\varepsilon_3/\varepsilon_1 = 2$ the anisotropy of B is significantly less pronounced and less interfacial energy density is required to counteract to that anisotropy to reach a comparable aspect ratio as shown in Figure 5a).

The two analytical approaches to the tetragonal inclusion problem discussed above both show, qualitatively and quantitatively, that for $\varepsilon_3/\varepsilon_1 \gg \infty$ the formation of plate-shaped precipitates is only driven by ε_3 . As indicated by the gray area in Figure 5a), the large uncertainty range of the misfit strain ratio for the γ'' phase fully lies within this limit!

Figure 6 shows the aspect ratio of the precipitates as a function of L for a realistic misfit ratio $\varepsilon_3/\varepsilon_1 = 60$. The aspect ratios of the plate-shaped precipitates increase with increasing L as the elastic bulk energy of the system dominates the interfacial part. The precipitate shapes were found to be ellipses with aspect ratios close to the prediction of Equation (25) and (26). The good agreement between the two-dimensional phase-field model and the three-dimensional analytical model in Figure 5a) and 6 suggests that a two-dimensional model is sufficient to describe the aspect ratio of a γ'' precipitate.

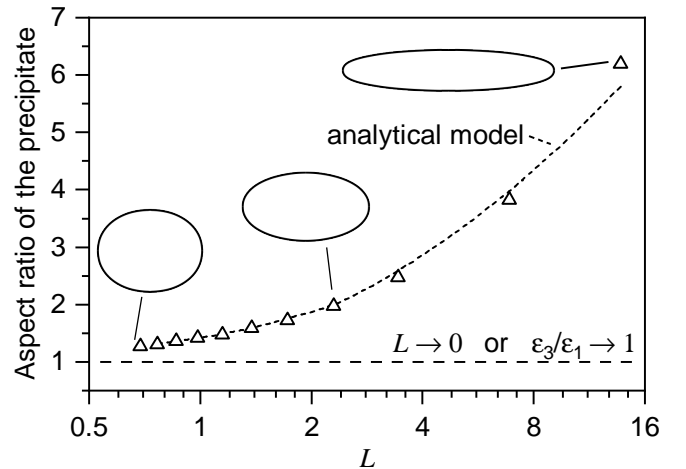


Figure 6. Precipitate aspect ratio as a function of L at $\varepsilon_3/\varepsilon_1 = 60$ considering isotropic elasticity and no elastic interaction with neighboring precipitates. Exemplary elliptical precipitate shapes are shown together with the prediction of the analytical model given in Equation (25) and (26).

Figure 7a) shows the influence of inhomogeneous elastic properties for precipitate and matrix phase on the precipitate shape as well as the influence of anisotropy of the elastic constants (see Table II). The simulation configuration is the same as in Figure 5a) with $\varepsilon_3/\varepsilon_1 = 60$ and $L = 4$. For reference, the circular shape of a precipitate with an isotropic misfit ($\varepsilon_1 = \varepsilon_3 = 30 \cdot 10^{-3}$) and isotropic homogeneous elasticity is given. In the considered case inhomogeneous elastic properties do not influence the precipitate shapes significantly. Anisotropic elastic properties lead to an elliptical precipitate with a reduced aspect ratio.

Figure 7b) shows the elastic energy density $B(\vec{n})$ (see Equation (27)) for isotropic and tetragonally anisotropic elastic constants (see Table II) and $\varepsilon_3/\varepsilon_1 = 60$. The tetragonal anisotropy of the γ'' phase leads to the [100] direction being elastically softer than in the isotropic case. For tilted directions orientations $\langle 10h \rangle$ B changes non-uniformly. The ratio of $B_{[100]}/B_{[001]}$ does not change significantly compared to the ratio $B_{[100]}/B_{\langle 10h \rangle}$ with $h \neq \{0, 1\}$. This qualitative change in the energetics of tilted interfaces leads to the observed shortening of the precipitate when anisotropy of the elastic properties is considered.

We conclude that without elastic interaction the formation of plate-shaped γ'' precipitate shapes is mainly driven by the tetragonally anisotropic misfit in the system. The aspect ratio of the precipitates depends on the misfit strains and on the interfacial energy density. For realistically high misfit ratios $\varepsilon_3/\varepsilon_1 \gg 1$ no influence of the absolute value of ε_1 on the precipitate shape is found. Inhomogeneity of the elastic constants has negligible influence on the precipitate shapes. Anisotropic elastic properties lead to elliptical precipitates with decreased aspect ratios.

Precipitate superstructure and particle-particle interaction

A square simulation domain at realistically high phase contents eventually leads to precipitates coagulating. Rectangular simulation domains have to be set up to avoid that. The aspect ratio of the rectangular simulation domains will be discussed as part of the simulation configuration. In the following simulations elastic data of the phases is anisotropic, $L = 4$ and $\varepsilon_3/\varepsilon_1 = 60$ (see Table II and III). We describe the interaction between neighboring precipitates by the particle distance. It is defined as the distance between the centers of the precipitates in [001] or y - direction or two times the height of the simulation domain.

Figure 8 shows the results of a simulation study in a domain with a fixed aspect ratio of 2.5 and rectangular superstructure. The size of the initial elliptical precipitate was kept constant ($R = 100$ and $r = 34$ gridpoints)

and the relative size of the simulation domain was varied in order to model different particle distances. The aspect ratio of a particle increases by 35 % in a system when the particle distance is reduced from $3.8l$ to $1.6l$. Note that due to the conserved aspect ratio of the domain also the particle distance in x -direction is reduced simultaneously and the phase fraction is rising. Interestingly, the increase in the aspect ratio at high phase contents does not lead to a simple stretching of the particle but also to a deviation from the elliptical shape. The precipitate shape has reduced curvature along its major extent. Similar elastic interactions affecting the precipitate shape have been reported for γ/γ' with volume fractions up to 75 % [23]. Distant precipitates experience attraction and close precipitates are repulsed leading to an equilibrium matrix channel width between the precipitates [44, 83–85].

Figure 9 shows precipitate shapes influenced by elastic particle-particle interaction in different superstructures at a particle distance of $1.8l$. The determined precipitate shapes subject to different implicit superstructures illustrate the significant influence of long-range order on precipitate shapes. The area of all three shapes is equal. The shapes for rectangular and hexagonal_y arrangement can be approximated with ellipses. The superstructure hexagonal_y shortens the precipitate by 10 % but it remains an ellipse. The hexagonal_x arrangement leads to deviation from the elliptical shape visible due to the fact that the phase boundary of the precipitate “rectangular” is intersected twice by the phase boundary of “hexagonal_x”. The sites of the intersections are indicated by arrows.

Figure 10 shows the total energy density plotted against the domain aspect ratio for the three possible superstructures at a particle distance of $1.8l$. The hexagonal_x arrangement is the energetically most favorable. The rectangular arrangement is intermediate and the hexagonal_y superstructure shows the highest energy density. The rectangular and the hexagonal_y superstructure both exhibit a steadily dropping energy density for aspect ratios of the simulation domain close to 1. It is only in the energetically most favorable hexagonal_x arrangement that one finds a distinct minimum at an aspect ratio of the simulation domain of 1.8. The implied microstructure of such an energetically optimum configuration is also given in Figure 10. For spherical precipitates with an isotropic misfit a cubic arrangement was found to be the energetic optimum [16].

The configuration that was found to be the energetically most favorable is the one where precipitates exhibit the largest distance to their nearest neighbors in the direction of the highest misfit strain ε_3 . An effect of the high elastic energy contribution in the hexagonal_y arrangement is visible in Figure 9, where it leads to additional shortening of the precipitate. Being the energetically minimum configuration of the presented model a

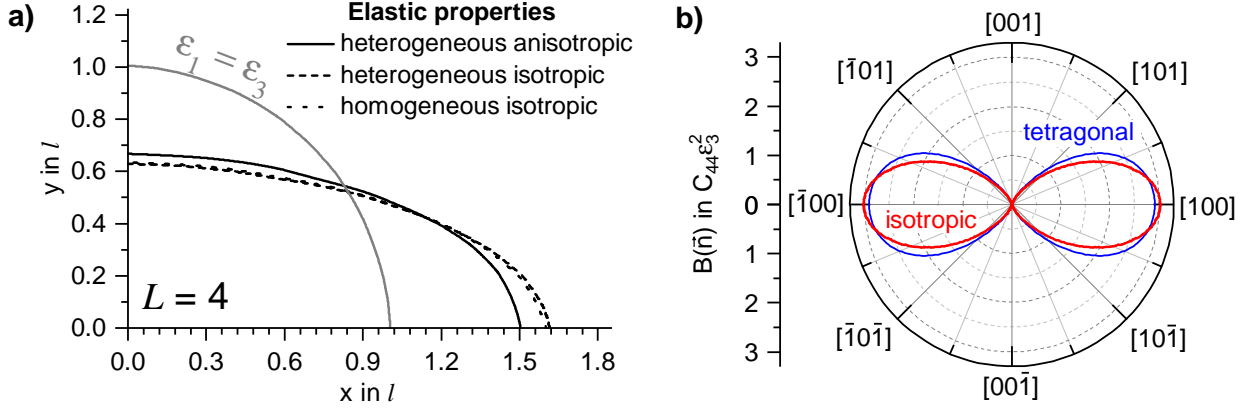


Figure 7. a) Influence of inhomogeneity and anisotropy of the elastic properties on precipitate shapes at $L = 4$. Elastic constants are given in Table II. For reference, the circular shape of a precipitate with $\epsilon_1 = \epsilon_3 = 30 \cdot 10^{-3}$ and isotropic homogeneous elasticity is shown. b) Polar plots of the orientation dependent elastic energy function $B(\vec{n})$ in the (010) plane for isotropic and tetragonal elastic constants ϵ_3/ϵ_1 .

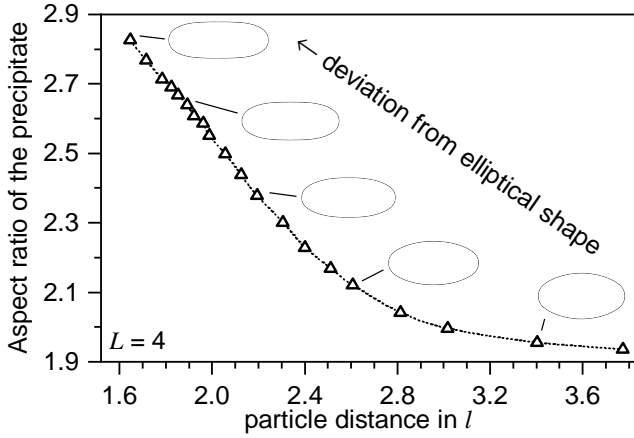


Figure 8. Dependence of the precipitate aspect ratio on the particle distance in y -direction with exemplary precipitate shapes. The aspect ratio of the simulation domain is 2.5. With increasing γ'' volume content, the aspect ratio increases and the precipitates deviate from their elliptical shape.

hexagonal_x superstructure with a domain aspect ratio of 1.8 will be used to describe a realistic single-variant γ/γ'' microstructure with a realistic volume fraction.

Energy density of the γ/γ'' interface

To reproduce experimentally observed aspect ratios of γ'' precipitates, we set up a simulation study assuming constant misfit strains and isotropic interfacial energy density. The simulation domain has an aspect ratio of 1.8, the initial particle has a radius of 20 gridpoints and a hexagonal_x superstructure was used. The sizes of the respective simulation domains were set such that they resemble a realistic γ'' volume fraction of 12%. We

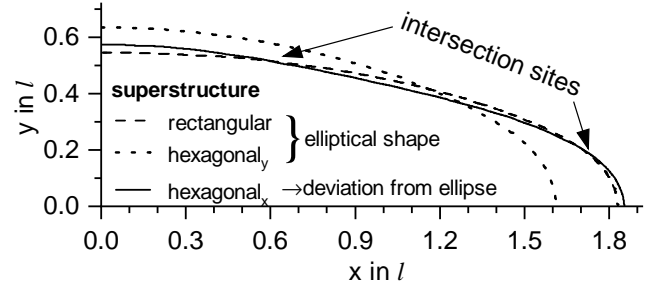


Figure 9. Equilibrium shapes of precipitates subject to different boundary conditions implying three superstructures. The superstructure nomenclature is introduced in Figure 4. Arrows indicate intersections of the elliptical shape outline (rectangular) with the non-elliptical shape (hexagonal_x).

approximate the volume fraction as the ratio between the volume of a spheroid with the same aspect ratio as the two-dimensional shape and the volume of a respective three-dimensional simulation domain by exploiting the system's four-fold rotational symmetry around the tetragonal axis. The approximated volume content \tilde{V} is then given by

$$\tilde{V} = \frac{4\pi}{3Ad^3\sqrt{1.8}}, \quad (28)$$

where A is the aspect ratio of the precipitate and d is the particle distance normalized by l . As shown in Figure 9 the precipitate shapes deviate from the elliptical shape and therefore assuming a spheroidal precipitate as in Equation (28) is not accurate. We assume that this inaccuracy is negligible as the inaccuracy of the volume content measurement itself is comparably large. Note that the single-variant microstructure discussed in this work reflects material aged under load for several hours

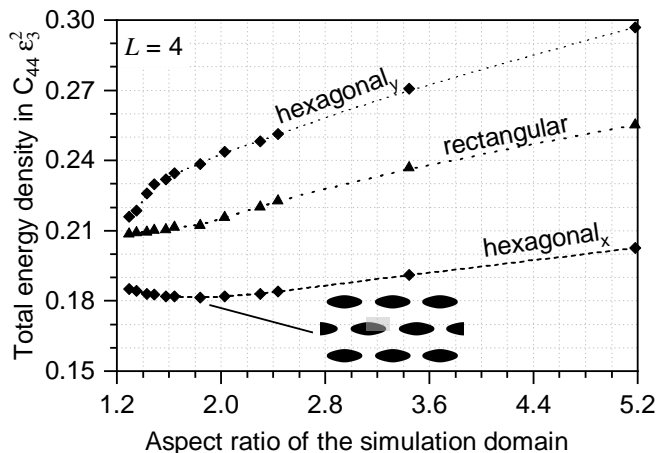


Figure 10. Mean energy densities of systems plotted against the domain aspect ratio. Results are shown for a particle distance of $1.8l$ and three different superstructures each. The superstructure nomenclature is introduced in Figure 4. The energetically most favorable microstructure is plotted.

[38, 86] or specifically tailored material [14]. We assume that particle interactions of perpendicularly oriented precipitates lead to the same stretching of the precipitates but might impose further constraint to the growth of precipitates that is not reflected by the proposed model.

Figure 11a) shows experimental data from various sources reporting the aspect ratio of γ'' precipitates as a function of the precipitate major radius [25, 49, 87, 88]. Interfacial dislocations occur when full coherency of precipitates larger than $R = 25$ nm is lost [25, 48, 49]. Here, we restrict to fully coherent precipitates, as interfacial dislocations alter the strain field around a precipitate [39] in a way that is not reflected by the model. The aspect ratio of the precipitates increase with increasing precipitate size due to the rising importance of elastic bulk effects over the interfacial energy with $L \sim l$ (see Equation (24)). In simulations with a particle distance of $5l$ an interfacial energy density of 65 mJ m^{-2} to 130 mJ m^{-2} is necessary to reproduce experimentally observed aspect ratios. This is in good accordance with the previously reported isotropic γ/γ'' interfacial energy density of $95 \pm 17 \text{ mJ m}^{-2}$ [25]. This value was obtained by the application of an analytical model for the equilibrium aspect ratio of a γ'' precipitate given in Equation (25) and (26) based on Eshelby's inclusion theory [48, 80]. This model assumes isotropic and homogeneous elasticity, isotropic interfacial energy density, a spheroidal precipitate shape and no elastic interaction. The prediction of this model for the size dependent aspect ratio of a precipitate with an interfacial energy density of 90 mJ m^{-2} is also shown in Figure 11a). An interfacial energy density of 145 mJ m^{-2} was found for D0_{22} precipitates in a Fe-Ni-Ta alloy [48].

Figure 11a) shows that at a realistic volume fraction

of 12% the isotropic energy density needed to reproduce experimental findings lies between 90 mJ m^{-2} and 200 mJ m^{-2} , which corresponds to $0.8 < L < 5.4$. In a real system the interfacial energy of a tetragonal to cubic interface might be strongly anisotropic [89, 90], which could also be included in a phase-field model. As to the best of our knowledge, no information about the magnitude of such an anisotropy for the coherent γ/γ'' -interface is available, we assume an isotropic Γ . The obtained isotropic interfacial energy densities are a factor of 1.5 higher than those determined without consideration of elastic particle-particle interaction. Figure 11a) includes data from averaged aspect ratios generated from TEM images as for example given in Figure 1b). 72 fully coherent γ'' precipitates in IN718M were evaluated by image analysis. The samples were homogenized at 1423 K for 2 h and subsequently water quenched. The error bar shows the standard deviation of the aspect ratio. For this system, we predict an isotropic interfacial energy density of 220 mJ m^{-2} .

Figure 11b) illustrates the influence of the competing factors discussed above on the aspect ratio of a precipitate. A higher the interfacial energy density Γ provides a tendency towards more spherical precipitates, i.e. smaller aspect ratios. Stronger elastic interactions between precipitates at higher volume fraction V , in turn, lead to higher precipitate aspect ratios (see Figure 11a). To estimate the interfacial energy density from the experimentally observed aspect ratios of precipitates it is crucial to take into account the elastic interactions of precipitates at finite volume fractions.

Comparison of theoretically determined equilibrium shapes with experimentally observed shapes is a possible way to get information about the interfacial energy [24–26]. However, the accuracy of this method is limited by the underlying model description of the equilibrium shape and by the possibility to experimentally observe precipitates in their equilibrium. The model presented in this work is in many ways an improvement over existing analytical models as it takes into account elastic interactions between precipitates in a two-dimensional optimum, non-rectangular arrangement and tetragonal/cubic anisotropy of the elastic constants for both phases. It is limited by being only a realistic description of a uniform single-variant microstructure that does not take into account the kinetics of precipitate growth that might have strong influence on the shapes of experimentally observed precipitates [91]. It was also found that a periodic arrangement of precipitates must not always be a stable configuration [46].

CONCLUSION

We evaluate influencing factors on equilibrium shapes of γ'' precipitates in Ni-based superalloys considering one

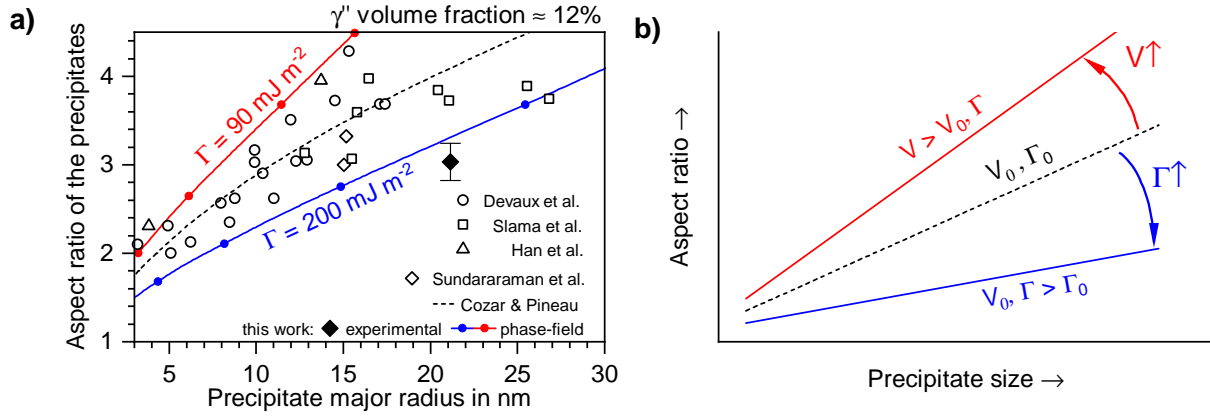


Figure 11. a) Data set of precipitate aspect ratio over major radius in the regime of fully coherent interfaces [25, 49, 87, 88]. Simulation-based estimates for a lower and upper boundary of the interfacial energy density are given for a γ'' volume fraction of 12%. The prediction of the size dependent aspect ratio of γ'' precipitates with an interfacial energy of 90 mJ m^{-2} by the analytical model of Cozar & Pineau is also shown [48]. b) Schematic plot illustrating the competing effects of volume fraction V and interfacial energy density Γ on the precipitate aspect ratio.

orientational variant. The shapes are determined using a phase-field formulation taking into account interfacial and elastic energy contributions.

1. At negligible elastic particle-particle interaction, the phase-field model provides elliptic equilibrium shapes γ'' that are fully consistent with former analytic descriptions [48, 80]. The aspect ratio R/r of a precipitate increases with increasing misfit strain ε_3 . The precipitate shape is influenced by ε_1 only for $\varepsilon_3/\varepsilon_1 \leq 3$. Inhomogeneity and anisotropy of the elastic constants have less significant influence on the γ'' precipitate shape.
2. Elastic particle-particle interactions significantly influence precipitate shapes at realistically high volume fractions. Different periodic arrangements of γ'' precipitates are modeled by respectively tailored boundary conditions. A decreased particle distance leads to an increased precipitate aspect ratio.
3. Non-volume conserving displacement boundary conditions allow precise determination of the total energy density of periodic precipitation microstructures. The energetically most favorable superstructure is a hexagonal_x precipitate arrangement (see Figure 4c).
4. The evaluation of interfacial energy density based on equilibrium shapes is sensitive to the phase content. At a realistic volume fraction of 12%, an interfacial energy density between 90 and 200 mJ m^{-2} leads to precipitate aspect ratios that match experimental observations. Respective interfacial energy densities determined without accounting for elastic interaction between the precipitates are 30% lower.

CREDIT AUTHORSHIP CONTRIBUTION STATEMENT

F. Schleifer: Conceptualization, Methodology, Software, Validation, Formal Analysis, Investigation, Writing – Original Draft, Visualization. **M. Holzinger:** Conceptualization, Methodology, Software. **Y.-Y. Lin:** Conceptualization, Investigation, Data Curation, Validation. **U. Glatzel:** Supervision, Resources, Writing – Review & Editing, Project Administration, Funding Acquisition. **M. Fleck:** Conceptualization, Software, Supervision, Writing – Review & Editing, Project Administration, Funding Acquisition.

DECLARATION OF COMPETING INTEREST

Authors have no conflict of interest to declare.

ACKNOWLEDGEMENTS

This work is funded by the Deutsche Forschungsgemeinschaft (DFG) in the priority program SPP 1713 (GL181/53-1|FL826/3-1). We thank the Federal Ministry of Education and Research (BMBF) for the financial support under the running project ParaPhase (funding code: 01IH15005B). The financial support of the Federal Ministry for Economics and Energy (BMWi) of the Federal Republic of Germany under the running project COORETEC: ISar (funding code: 03ET7047D) is greatly acknowledged. We thank our former colleague F. Krieg for the provision of RUS data and A. Finel from ONERA in Châtillon, France for the discussion on tetragonal anisotropy.

- * michael.fleck@uni-bayreuth.de
- [1] D. F. Paulonis, J. M. Oblak, D. S. Duvall, Precipitation in Nickel-base Alloy 718., Amer. Soc. Metals, Trans. Quart. 62 (1969) 611–622.
 - [2] I. Kirman, D. H. Warrington, The Precipitation of Ni₃Nb Phases in a Ni-Fe-Cr-Nb Alloy, Metallurgical Transactions 1 (1970) 2667–2675.
 - [3] K. Kusabiraki, I. Hayakawa, S. Ikeuchi, T. Ooka, Morphology of γ'' precipitates in Ni-18Cr-16Fe-5Nb-3Mo Alloy, Iron and Steel (1994) 348–352.
 - [4] K. Kusabiraki, I. Hayakawa, S. Keuchi, T. Ooka, Lattice Constants of γ and γ'' Phases and γ''/γ Lattice Mismatches in a Ni-15Cr-8-Fe-6Nb Alloy, ISIJ 36 (1996) 310–316.
 - [5] K. Kusabiraki, T. Tsutsumi, S. Saji, Effects of cold rolling and annealing on the structure of γ'' precipitates in a Ni-18Cr-16Fe-5Nb-3Mo alloy, Metallurgical and Materials Transactions A 30 (1999) 1923–1931.
 - [6] A. J. Detor, R. DiDomizio, R. Sharghi-Moshtaghin, N. Zhou, R. Shi, Y. Wang, D. P. McAllister, M. J. Mills, Enabling Large Superalloy Parts Using Compact Coprecipitation of γ' and γ'' , Metallurgical and Materials Transactions A 49 (2018) 708–717.
 - [7] R. Shi, D. P. McAllister, N. Zhou, A. J. Detor, R. DiDomizio, M. J. Mills, Y. Wang, Growth behavior of γ'/γ'' coprecipitates in Ni-Base superalloys, Acta Materialia 164 (2019) 220–236.
 - [8] P. M. Mignanelli, N. G. Jones, E. J. Pickering, O. M. Messé, C. M. Rae, M. C. Hardy, H. J. Stone, Gamma-gamma prime-gamma double prime dual-superlattice superalloys, Scripta Materialia 136 (2017) 136–140.
 - [9] P. M. Mignanelli, N. G. Jones, M. C. Hardy, H. J. Stone, On the Time-Temperature-Transformation Behavior of a New Dual-Superlattice Nickel-Based Superalloy, Metallurgical and Materials Transactions A 49 (2018) 699–707.
 - [10] K. N. Amato, S. M. Gaytan, L. E. Murr, E. Martinez, P. W. Shindo, J. Hernandez, S. Collins, F. Medina, Microstructures and mechanical behavior of Inconel 718 fabricated by selective laser melting, Acta Materialia 60 (2012) 2229–2239.
 - [11] C. Y. Yap, C. K. Chua, Z. L. Dong, Z. H. Liu, D. Q. Zhang, L. E. Loh, S. L. Sing, Review of selective laser melting: Materials and applications, Applied Physics Reviews 2 (2015) 041101.
 - [12] J. Ströckner, M. Terock, U. Glatzel, Mechanical and Microstructural Investigation of Nickel-Based Superalloy IN718 Manufactured by Selective Laser Melting (SLM), Advanced Engineering Materials 17 (2015) 1099–1105.
 - [13] T. Trosch, J. Ströckner, R. Völkl, U. Glatzel, Microstructure and mechanical properties of selective laser melted Inconel 718 compared to forging and casting, Materials Letters 164 (2016) 428–431.
 - [14] H. Zhang, C. Li, Q. Guo, Z. Ma, H. Li, Y. Liu, Improving creep resistance of nickel-based superalloy Inconel 718 by tailoring gamma double prime variants, Scripta Materialia 164 (2019) 66–70.
 - [15] A. Khachaturyan, Some questions concerning the theory of phase transformations in solids, Soviet Phys. Solid State 8 (1967) 2163–2168.
 - [16] A. Khachaturyan, V. Airapetyan, Spatially periodic distributions of new phase inclusions caused by elastic distortions, Physica status solidi (a) 26 (1974) 61–70.
 - [17] W. C. Johnson, J. W. Cahn, Elastically Induced Shape Bifurcations, Acta Metallurgica 32 (1984) 1925–1933.
 - [18] P. W. Voorhees, G. B. McFadden, W. C. Johnson, On the morphological development of second-phase particles in elastically-stressed solids, Acta Metallurgica Et Materialia 40 (1992) 2979–2992.
 - [19] M. E. Thompson, C. S. Su, P. W. Voorhees, The equilibrium shape of a misfitting precipitate, Acta Metallurgica Et Materialia 42 (1994) 2107–2122.
 - [20] M. E. Thompson, P. W. Voorhees, Equilibrium particle morphologies in elastically stressed coherent solids, Acta Materialia 47 (1999) 983–996.
 - [21] X. Li, K. Thornton, Q. Nie, P. W. Voorhees, J. S. Lowengrub, Two- and three-dimensional equilibrium morphology of a misfitting particle and the Gibbs-Thomson effect, Acta Materialia 52 (2004) 5829–5843.
 - [22] I. Schmidt, D. Gross, The equilibrium shape of an elastically inhomogeneous inclusion, Journal of the Mechanics and Physics of Solids 45 (1997) 1521–1549.
 - [23] R. Mueller, S. Eckert, D. Gross, 3D equilibrium shapes of periodically arranged anisotropic precipitates with elastic misfit, Archives of Mechanics 52 (2000) 663–683.
 - [24] V. Lanteri, T. Mitchell, A. H. Heuer, Morphology of tetragonal precipitates in partially stabilized ZrO₂, Journal of the American Ceramic Society 69 (1986) 564–569.
 - [25] A. Devaux, L. Nazé, R. Molins, A. Pineau, A. Organista, J. Y. Guédou, J. F. Uginet, P. Héritier, Gamma double prime precipitation kinetic in Alloy 718, Materials Science and Engineering: A 486 (2008) 117–122.
 - [26] M. Holzinger, F. Schleifer, U. Glatzel, M. Fleck, Phase-field modeling of γ' -precipitate shapes in nickel-base superalloys and their classification by moment invariants, European Physical Journal B 92 (2019).
 - [27] L.-Q. Chen, Phase field models for microstructure evolution, Annual Review of Materials Research 32 (2002) 113–140.
 - [28] M. Asta, C. Beckermann, A. Karma, W. Kurz, R. Napolitano, M. Plapp, G. Purdy, M. Rappaz, R. Trivedi, Solidification microstructures and solid-state parallels: Recent developments, future directions, Acta Materialia 57 (2009) 941.
 - [29] I. Steinbach, Phase-field models in materials science, Modelling Simul. Mater. Sci. Eng. 17 (2009) 73001.
 - [30] Y. Wang, J. Li, Phase field modeling of defects and deformation, Acta Materialia 58 (2010) 1212.
 - [31] S. DeWitt, K. Thornton, Phase field modeling of microstructural evolution, in: Computational Materials System Design, Springer, 2018, pp. 67–87.
 - [32] Y. Wang, D. Banerjee, C. Su, A. Khachaturyan, Field kinetic model and computer simulation of precipitation of L12 ordered intermetallics from fcc solid solution, Acta Materialia 46 (1998) 2983–3001.
 - [33] J. Zhu, T. Wang, A. Ardell, S. Zhou, Z. Liu, L. Chen, Three-dimensional phase-field simulations of coarsening kinetics of γ' particles in binary Ni-Al alloys, Acta Materialia 52 (2004) 2837–2845.
 - [34] A. Gaubert, Y. Le Bouar, A. Finel, Coupling phase field and viscoplasticity to study rafting in Ni-based superalloys, Philosophical Magazine 90 (2010) 375.
 - [35] L. T. Mushongera, M. Fleck, J. Kundin, Y. Wang, H. Emmerich, Effect of Re on directional γ' -coarsening in commercial single crystal Ni-base superalloys: A phase field study, Acta Materialia 93 (2015) 60–72.

- [36] Y. Pang, Y. S. Li, X. Wu, W. Liu, Z. Hou, Phase-field simulation of diffusion-controlled coarsening kinetics of γ' phase in Ni-Al alloy, *International Journal of Materials Research* 106 (2015) 108–113.
- [37] M. S. Bhaskar, Quantitative phase field modelling of precipitate coarsening in Ni-Al-Mo alloys, *Computational Materials Science* 146 (2018) 102–111.
- [38] N. Zhou, D. C. Lv, H. L. Zhang, D. McAllister, F. Zhang, M. J. Mills, Y. Wang, Computer simulation of phase transformation and plastic deformation in IN718 superalloy: Microstructural evolution during precipitation, *Acta Materialia* 65 (2014) 270.
- [39] Y. Ji, Y. Lou, M. Qu, J. D. Rowatt, F. Zhang, T. W. Simpson, L.-Q. Chen, Predicting Coherency Loss of γ'' Precipitates in IN718 Superalloy, *Metallurgical and Materials Transaction A* 47 (2016) 3235.
- [40] Y. Wang, L.-Q. Chen, A. Khachaturyan, Shape evolution of a precipitate during strain-induced coarsening: a computer simulation, *Scripta Metallurgica et Materialia* 25 (1991) 1387–1392.
- [41] Y. Wang, L.-Q. Chen, A. Khachaturyan, Kinetics of strain-induced morphological transformation in cubic alloys with a miscibility gap, *Acta Metallurgica et Materialia* 41 (1993) 279–296.
- [42] P. H. Leo, J. S. Lowengrub, H.-J. Jou, A diffuse interface model for microstructural evolution in elastically stressed solids, *Acta Materialia* 46 (1998) 2113–2130.
- [43] M. Cottura, Y. Le Bouar, B. Appolaire, A. Finel, Rôle of elastic inhomogeneity in the development of cuboidal microstructures in Ni-based superalloys, *Acta Materialia* 94 (2015) 15–25.
- [44] A. M. Jokisaari, S. S. Naghavi, C. Wolverton, P. W. Voorhees, O. G. Heinonen, Predicting the morphologies of γ' precipitates in cobalt-based superalloys, *Acta Materialia* 141 (2017) 273–284.
- [45] B. Bhadak, R. Sankarasubramanian, A. Choudhury, Phase-Field Modeling of Equilibrium Precipitate Shapes Under the Influence of Coherency Stresses, *Metallurgical and Materials Transactions A* 49 (2018) 5705–5726.
- [46] M. Degeiter, Y. Le Bouar, B. Appolaire, M. Perrut, A. Finel, Instabilities in the periodic arrangement of elastically interacting precipitates in nickel-base superalloys, *Acta Materialia* 187 (2020) 41–50.
- [47] C. Slama, M. Abdellaoui, Structural characterization of the aged Inconel 718, *Alloys and Compounds* 306 (2000) 277–284.
- [48] R. Cozar, A. Pineau, Influence of coherency strains on precipitate shape in a FeNiTa alloy, *Scripta Metallurgica* 7 (1973) 851–854.
- [49] C. Slama, C. Servant, G. Cizeron, Aging of the Inconel 718 alloy between 500 and 750 °C, *Journal of Materials Research* 12 (1997) 2298–2316.
- [50] D. Connétable, M. Mathon, J. Lacaze, First principle energies of binary and ternary phases of the Fe-Nb-Ni-Cr system, *Calphad: Computer Coupling of Phase Diagrams and Thermochemistry* 35 (2011) 588–593.
- [51] S. Dai, W. Liu, First-principles study on the structural, mechanical and electronic properties of δ and γ'' phases in Inconel 718, *Computational Materials Science* 49 (2010) 414–418.
- [52] I. J. Moore, M. G. Burke, E. J. Palmiere, Modelling the nucleation, growth and coarsening kinetics of γ'' ($D0_{22}$) precipitates in the Ni-base Alloy 625, *Acta Materialia* 119 (2016) 157–166.
- [53] G. Simmons, *Single Crystal Elastic Constants and Calculated Aggregate Properties*, Southern Methodist University, Dallas, Texas, 1965.
- [54] F. Luo, X.-R. Chen, L.-C. Cai, Q. Wu, Thermoelastic properties of nickel from molecular dynamic simulations, *Journal of Atomic and Molecular Science* 2 (2011) 10–19.
- [55] M. Fleck, F. Schleifer, M. Holzinger, U. Glatzel, Phase-Field Modeling of Precipitation Growth and Ripening During Industrial Heat Treatments in Ni-Base Superalloys, *Metallurgical and Materials Transactions A* 49 (2018) 4146–4157.
- [56] J. W. Brooks, P. J. Bridges, Metallurgical stability of INCONEL alloy 718, in: *Superalloys*, TMS, 1988, pp. 33–42.
- [57] F. Theska, A. Stanojevic, B. Oberwinkler, S. P. Ringer, S. Primig, On conventional versus direct ageing of Alloy 718, *Acta Materialia* 156 (2018) 116–124.
- [58] R. Lawitzki, S. Hassan, L. Karge, J. Wagner, D. Wang, J. von Kobylinski, C. Kremaszky, M. Hofmann, R. Gilles, G. Schmitz, Differentiation of γ' - and γ'' - precipitates in Inconel 718 by a complementary study with small-angle neutron scattering and analytical microscopy, *Acta Materialia* 163 (2019) 28–39.
- [59] R. Cozar, A. Pineau, Morphology of γ' and γ'' precipitates and thermal stability of Inconel 718 type alloys, *Metallurgical Transactions* 4 (1973) 47–59.
- [60] J. M. Oblak, D. F. Paulonis, D. S. Duvall, Coherency Strengthening in Ni Base Alloys Hardened by $D0_{22}$ γ'' Precipitate, *Metall. Trans.* 5 (1974) 143.
- [61] M. C. Chaturvedi, Y.-F. Han, Strengthening mechanism in Inconel 718 superalloy, *Metal Science* 17 (1983) 145–149.
- [62] R. Y. Zhang, Z. N. Bi, H. L. Qin, J. Zhang, A. D. Fortes, Constrained Lattice Misfit Measurement in Bulk Inconel 718 Using High Resolution Neutron Diffraction, in: *Proceedings of the 9th International Symposium on Superalloy 718 & Derivatives: Energy, Aerospace, and Industrial Applications*, 2018, pp. 439–448.
- [63] R. Völkl, U. Glatzel, M. Feller-Kniepmeier, Measurement of the lattice misfit in the single crystal nickel based superalloys CMSX-4, SRR99 and SC16 by convergent beam electron diffraction, *Acta Materialia* 46 (1998) 4395–4404.
- [64] R. Völkl, U. Glatzel, M. Feller-Kniepmeier, Measurement of the Unconstrained Misfit in the Nickel-Base Superalloy CMSX-4 with CBED, *Scripta Materialia* 38 (1998) 893–900.
- [65] L. Müller, U. Glatzel, M. Feller-Kniepmeier, Calculation of the internal stresses and strains in the microstructure of a single crystal nickel-base superalloy during creep, *Acta Metallurgica et Materialia* 41 (1993) 3401–3411.
- [66] M. Plapp, Unified derivation of phase-field models for alloy solidification from a grand-potential functional, *Physical Review E* 84 (2011) 31601.
- [67] L. T. Mushongera, M. Fleck, J. Kundin, F. Querfurth, H. Emmerich, Phase-field study of anisotropic γ' -coarsening kinetics in Ni-base superalloys with varying Re and Ru contents, *Advanced Engineering Materials* 17 (2015) 1149.
- [68] A. Finel, Y. Le Bouar, B. Dabas, B. Appolaire, Y. Yamada, T. Mohri, Sharp Phase Field Method, *Physical Review Letters* 121 (2018) 25501.
- [69] M. Fleck, F. Schleifer, U. Glatzel, Frictionless motion of marginally resolved diffuse interfaces in phase-field mod-

- eling, arXiv preprint arXiv:1910.05180 (2019).
- [70] K. Kassner, C. Misbah, J. Müller, J. Kappey, P. Kohlert, Phase-field modeling of stress-induced instabilities, *Physical Review E* 63 (2001) 36117.
- [71] M. Fleck, E. A. Brener, R. Spatschek, B. Eidel, Elastic and plastic effects on solid-state transformations: A phase field study, *International Journal of Materials Research* 101 (2010) 462–466.
- [72] A. Durga, P. Wollants, N. Moelans, Evaluation of interfacial excess contributions in different phase-field models for elastically inhomogeneous systems, *Modell. Sim. Mater. Sci. Eng.* 21 (2013) 55018.
- [73] M. Fleck, L. Mushongera, D. Pilipenko, K. Ankit, H. Emmerich, On phase-field modeling with a highly anisotropic interfacial energy, *Eur. Phys. J. Plus* 126 (2011) 95.
- [74] B. Nestler, F. Wendler, M. Selzer, B. Stinner, H. Garcke, Phase-field model for multiphase systems with preserved volume fractions, *Physical Review E* 78 (2008) 11604.
- [75] U. Glatzel, M. Feller-Kniepmeier, Calculations of internal stresses in the γ/γ' microstructure of a nickel-base superalloy with high volume fraction of γ' -phase, *Scripta Metallurgica* 23 (1989) 1839–1844.
- [76] M. Probst-Hein, A. Dlouhy, G. Eggeler, Interface dislocations in superalloy single crystals, *Acta Materialia* 47 (1999) 2497–2510.
- [77] J. Preußner, Y. Rudnik, R. Völkl, U. Glatzel, Finite-element modelling of anisotropic single-crystal superalloy creep deformation based on dislocation densities of individual slip systems, *Zeitschrift für Metallkunde* 96 (2005) 595–601.
- [78] T. Pollock, A. Argon, Intermediate Temperature Creep Deformation in CMSX-3 Single Crystals, in: *Superalloys*, 1988, pp. 285–294.
- [79] S. Gurevich, A. Karma, M. Plapp, R. Trivedi, Phase-field study of three-dimensional steady-state growth shapes in directional solidification, *Physical Reviews E* 81 (2010) 11603.
- [80] J. D. Eshelby, The determination of the elastic field of an ellipsoidal inclusion and related problems, *Proceedings of the Royal Society of London. Series A. Mathematical and Physical Sciences* 241 (1957) 376–396.
- [81] J. Morris Jr, The Khachaturyan theory of elastic inclusions: Recollections and results, *Philosophical Magazine* 90 (2010) 3–35.
- [82] S. Wen, E. Kostlan, M. Hong, A. Khachaturyan, J. Morris Jr, The preferred habit of a tetragonal inclusion in a cubic matrix, *Acta Metallurgica* 29 (1981) 1247–1254.
- [83] C. H. Su, P. W. Voorhees, The Dynamics of Precipitate Evolution in Elastically Stressed Solids - I. Inverse Coarsening, *Acta Metallurgica* 44 (1996) 2001–2016.
- [84] C. H. Su, P. W. Voorhees, The Dynamics of Precipitate Evolution in Elastically Stressed Solids - II. Particle Alignment, *Acta Metallurgica* 44 (1996) 1987–1999.
- [85] J. V. Goerler, I. Lopez-Galilea, M. L. Roncery, O. Shchyglo, W. Theisen, I. Steinbach, Topological phase inversion after long-term thermal exposure of nickel-base superalloys: Experiment and phase-field simulation, *Acta Materialia* 124 (2017) 151–158.
- [86] M. Gao, S. Chen, D. Gary Harlow, R. P. Wei, Preferential coarsening of γ'' precipitates in INCONEL 718 during creep, *Metallurgical and Materials Transactions A* 27 (1996) 3391–3398.
- [87] Y.-F. Han, P. Deb, M. C. Chaturvedi, Coarsening behaviour of γ'' - and γ' -particles in Inconel alloy 718, *Metal Science* 16 (1982) 555–562.
- [88] M. Sundararaman, P. Mukhopadhyay, S. Banerjee, Some aspects of the precipitation of metastable intermetallic phases in INCONEL 718, *Metallurgical Transactions* 23 A (1992) 2015–2028.
- [89] V. Vaithyanathan, C. Wolverton, L. Chen, Multiscale modeling of θ' precipitation in Al-Cu binary alloys, *Acta Materialia* 52 (2004) 2973–2987.
- [90] K. Kim, A. Roy, M. Gururajan, C. Wolverton, P. W. Voorhees, First-principles/Phase-field modeling of θ' precipitation in Al-Cu alloys, *Acta Materialia* 140 (2017) 344–354.
- [91] V. Vaithyanathan, C. Wolverton, L. Chen, Multiscale modeling of precipitate microstructure evolution, *Physical Review Letters* 88 (2002) 125503.